Shock-induced shear bands in an energetic molecular crystal: Application of shock-front absorbing boundary conditions to molecular dynamics simulations

M. J. Cawkwell* and Thomas D. Sewell†
Theoretical Division, Los Alamos National Laboratory, Los Alamos, New Mexico 87545, USA

Lianqing Zheng‡ and Donald L. Thompson§
Department of Chemistry, University of Missouri-Columbia, Columbia, Missouri 65211, USA
(Received 16 November 2007; revised manuscript received 13 June 2008; published 17 July 2008)

The response of the energetic molecular crystal cyclotrimethylene trinitramine (RDX) to the propagation of planar shock waves normal to (100) has been studied using large-scale molecular dynamics simulations that employ an accurate and transferable nonreactive potential. The propagation of the shock waves was simulated using nonequilibrium molecular dynamics. Shear bands were nucleated during shocks with a particle velocity of 1.0 km s^{-1} and corresponding Rankine-Hugoniot shock pressure of 9.7 GPa. These defects propagate into the compressed material at 45° to [100] in the [010] zone. The shear bands evolve slowly compared to the time scales routinely accessible to nonequilibrium molecular dynamics toward a liquidlike state as a result of viscous heating. A recently developed shock-front absorbing boundary condition [A. V. Bolesta *et al.*, Phys. Rev. B **76**, 224108 (2007)] was applied to the simulation cells at the moment of maximum compression to sustain the shock-compressed state. Molecular dynamics simulations were then employed to study the temporal and structural evolution of the shock-induced shear bands toward a steady-fluctuating state. Owing to the intense, viscous flow-driven heating within the shear bands, these defects can be considered to be homogeneously nucleated hot spots.

DOI: 10.1103/PhysRevB.78.014107 PACS number(s): 62.50.−p, 62.20.F−, 61.72.Bb, 61.20.Ja

I. INTRODUCTION

Defects in solid and crystalline energetic materials are known to exert a significant influence on impact and initiation sensitivity.[1] Mesoscopic and macroscopic defects lead to the spatial localization of the translational energy from a shock through, for example, the formation of jets during the collapse of voids[2,3] or interfacial friction at cracks or particle boundaries.[4,5] Events of this kind result in hot spots where temperature and/or stress may exceed significantly values in the bulk and hence promote molecular decomposition. The formation of hot spots through these mechanisms is well understood, at least on a qualitative level,[6] and apply in general to all solid energetic materials.

The impact sensitivity of defect-free single crystals of the energetic molecular crystal pentaerythritol tetranitrate (PETN) was found to depend strongly on the crystallographic orientation of the shock propagation direction.[7–9] In this case, dislocation-mediated plastic deformation was proposed as an explanation for the observed orientation dependencies. Slip systems were identified in single crystals using x-ray topography and by the analysis of slip traces after surface indentation.[10] Those orientations of the shock propagation direction for which there was no resolved shear stress on any slip system were found to have a high Hugoniot elastic limit and high impact sensitivity. Similarly, those orientations for which a shear stress was resolved on all of the slip systems identified experimentally were found to have low Hugoniot elastic limit and low impact sensitivity. Hence, in the absence of mesoscopic and macroscopic defects, extended crystal defects at the atomic or molecular scale were found to play a role in determining impact sensitivity. This work led to the formulation of the steric-hindrance model,[7,8,11] wherein an absence of dislocation-mediated plasticity for a given crystallographic orientation of the shock propagation direction promotes initiation since shear stresses cannot be relaxed easily and molecules deform severely, inducing bond-breaking events.

We have studied the response of single crystals of the widely used energetic molecular crystal cyclotrimethylene trinitramine, $C_3H_6N_6O_6$ (RDX), to the propagation of shock waves normal to (100) by means of large-scale molecular dynamics (MD) simulations, with particular focus on the shock-induced nucleation of extended defects. Under ambient pressure and temperature, RDX adopts an orthorhombic unit cell in space group *Pbca* that contains eight molecules (α-polymorph).[12] An RDX molecule is depicted in Fig. 1(a) and a projection of the α-RDX unit cell along [001] in Fig. 1(b). Three slip systems were identified in RDX single crystals by the analysis of slip traces after surface indentation: (010)[001], (021)[100], and $(02\bar{1})$[100].[10] Hence, the [100] shock propagation direction is special since there is no resolved shear stress on any of the slip systems identified un-

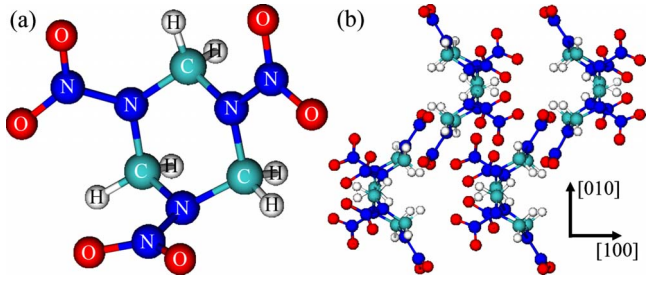

FIG. 1. (Color online) (a) An RDX molecule and (b) projection of the α-RDX unit cell along [001].

der quasistatic loading.[13] Thus, on the basis of the steric-hindrance model, we expect this orientation to be of high impact sensitivity. However, earlier work on (111)-oriented RDX single crystals revealed an abrupt change in the mechanism of plastic deformation above a certain shock pressure that could not have been anticipated based on either crystallographic arguments or the results of quasistatic loading experiments.[13,14] This work led us to the conclusion that extrapolating the mechanisms for plastic deformation identified in energetic molecular crystals under quasistatic loading over many orders of magnitude in strain rate can be rather unreliable, particularly for complicated, low-symmetry crystal structures. In fact, PETN can be considered as a special case in this regard since it adopts a relatively high-symmetry tetragonal unit cell comprising only two molecules.

Nonequilibrium molecular dynamics (NEMD) simulations[15–20] of the propagation of planar shock waves normal to (100) were performed for particle velocities $U_p = 0.63$ and 1.0 km s^{-1}, corresponding to shock pressures, P_{RH}, calculated using the Rankine-Hugoniot jump conditions[21] of 5.7 and 9.7 GPa, respectively. At $P_{\mathrm{RH}} = 5.7$ GPa, we found no evidence for the nucleation of crystal defects. However, at $P_{\mathrm{RH}} = 9.7$ GPa, liquidlike shear bands (SBs) were nucleated which propagate at 45° to the compression axis. The remainder of this paper is devoted to the characterization of these defects.

A popular method for generating planar shock waves in NEMD simulations is to either drive a rigid piston at a specified particle velocity onto a stationary simulation cell or impact a simulation cell onto a fixed, rigid piston at a specified particle velocity. In this paper we have employed the latter approach. Both of these methods limit the time interval over which material remains on the Hugoniot locus since once the shock wave reaches the free surface of the simulation cell, a rarefaction wave propagates rapidly back into the shock-compressed material. Hence, material near the free surface is on the Hugoniot locus for a very limited time. Simulations of this type typically employ simulation cells that are relatively long parallel to the shock propagation direction in order to maximize the time interval over which material in the vicinity of the piston is sustained in the shocked state. This approach is often not practical computationally, particularly in the simulation of slow processes such as plasticity or chemistry. In the present work, this limitation of NEMD simulation techniques is particularly pronounced since the internal structure of the shock-induced shear bands evolves relatively slowly, compared to typical NEMD time scales, by a viscous heating mechanism.

We have employed, with modifications, a simple and robust method for extending time scales in molecular dynamics simulations of shock loading that was first developed by Bolesta *et al.*[22] The shock-front absorbing boundary condition (SFABC) (Ref. 23) enables a seamless transition from a NEMD simulation of the propagation of a shock front to the simulation of shock-induced defects during their evolution toward a steady-fluctuating state. SFABCs capture the simulation cell at the point of maximum compression in a NEMD simulation and prevent the emission of rarefaction waves from the free surface. Furthermore, the SFABC approach obviates the requirement for simulation cells that are "long" parallel to the direction of shock propagation, does not introduce any incoherent interfaces into the system, and leaves unaffected the microcanonical equations of motion. The SFABC method and its application to a crystalline solid are described in detail in Sec. III.

Other methods for the absorption of waves incident at boundaries in MD simulations have been developed in recent years. For example, Namilae *et al.*[24] implemented a differential equation-based absorbing boundary condition (ABC) to match the impedance of a semi-infinite continuum space to that of an atomistic region. However, ABCs of this type are based on the linear wave equation and for this reason are not suited to the absorption of shock waves.

II. NONEQUILIBRIUM MOLECULAR DYNAMICS SIMULATIONS

The nonreactive, fully flexible molecular potential for nitramines developed by Smith and co-workers[25,26] was employed in all of the MD simulations. The Smith-Bharadwaj potential[25] describes bond stretches, bond angles, and out-of-plane bends using harmonic springs. Torsions are represented by anharmonic terms that display extrema at the torsion angles that correspond to stationary points on the conformational energy surface. The intramolecular terms were parametrized to quantum chemistry calculations of the structure, vibrational frequencies, and barriers to conformational change in a model compound, 1,3-dimethyl-1,3-dinitro methyldiamine. Intermolecular interactions are represented by a sum of Buckingham potentials parametrized to standard literature values. Electrostatic interactions are included explicitly and employ partial charges that were increased for all species by 25% compared to quantum chemistry-calculated values to account for the effects of polarization in condensed phases. The Smith-Bharadwaj potential,[25] while not parametrized to reproduce any particular property of condensed phase nitramines, was shown to provide excellent descriptions of crystalline cyclotetramethylene tetranitramine (HMX) (Refs. 26 and 27) and RDX. In the case of RDX the Smith-Bharadwaj potential[25] not only predicts the orthorhombic *Pbca* space group to be the crystal structure with the lowest free energy at zero pressure and 300 K but it also provides remarkably accurate predictions for its lattice parameters,[12] single-crystal elastic constants,[28] coefficient of thermal expansion,[29] and isothermal compression curve up to the α-to-γ phase transformation.[30] Furthermore, it predicts the P versus U_p Hugoniot of RDX crystals shock loaded normal to (111) to within 0.5 GPa of experiment.[31]

The lattice parameters of α-RDX calculated using the Smith-Bharadwaj potential[25] at 300 K and zero pressure are $a = 13.400$ Å, $b = 11.517$ Å, and $c = 10.623$ Å, each of which is within 1.7% of experiment.[12] These calculated lattice parameters were used for all the simulations reported here. NEMD simulations of the propagation of planar shock waves normal to (100) employed an oblong simulation cell measuring $120a \times 20b \times 20c$, containing 8.064×10^6 atoms. A shorter simulation cell measuring $60a \times 20b \times 20c$ was also used to study the effect of SFABCs on the structure of shock-induced defects. These cells are hereafter referred to

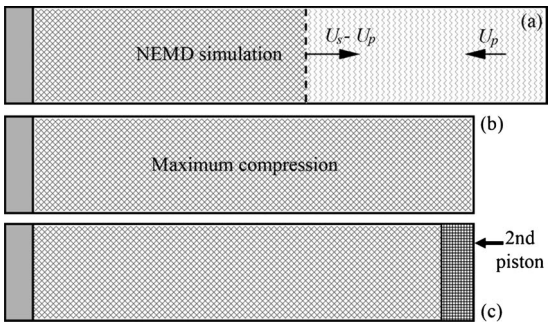

FIG. 2. (a) Schematic illustration of a NEMD shock loading simulation. The vertical broken line represents the position of the shock front which is traveling from left to right. (b) Simulation cell at maximum compression. (c) Application of the second piston in the shock-front absorbing boundary condition (SFABC) method.

as the long and short cells, respectively. Finally, we also created a quasi-two-dimensional (quasi-2D) simulation cell to assess and mitigate any finite-size effects on the defect structures generated during the simulations. The quasi-2D cell measured $149a \times 3b \times 141c$ and contained 10.6×10^6 atoms. An additional 200 Å thick vacuum region was included in the simulation cells along [100] to minimize electrostatic interactions between free surfaces upon the application of three-dimensional periodic boundary conditions. The simulation cells were thermalized until intermolecular and intramolecular temperatures equilibrated to 300 K prior to shock loading. The propagation of supported planar shock waves was simulated in the microcanonical ensemble by impacting the cells onto a fixed piston of thickness $3a$ consisting of rigid RDX molecules in the same crystallographic orientation as the simulation cell by adding to all atoms a particle velocity U_p parallel to [100]. This generates a shock wave propagating at velocity $U_w = U_s - U_p$ relative to the stationary piston, where U_s is the shock wave velocity; this is illustrated schematically in Fig. 2(a). All simulations were performed using the LAMMPS code.[32] Long-range electrostatic interactions were calculated using the PPPM method[33] and all C-H bonds were constrained to equilibrium length using the SHAKE algorithm. One NEMD simulation was performed at $U_p = 0.63$ km s^{-1} using the long cell and three at $U_p = 1.0$ km s^{-1} using the long, short, and quasi-2D cells. A 0.4 fs time step for the integration of the equations of motion was employed in each case.

III. SHOCK-FRONT ABSORBING BOUNDARY CONDITIONS

The SFABC method facilitates a seamless transition from a NEMD simulation of the propagation of a shock wave through a medium to a MD simulation of the evolution of any defects created by the shock wave. SFABCs were originally implemented and applied to MD studies of shock waves in reactive methane.[22] In the present work on crystalline RDX, we used a modest simplification of the original method for absorbing the shock front which we expect to be more robust in its implementation. The SFABC method is illustrated schematically in Fig. 2.

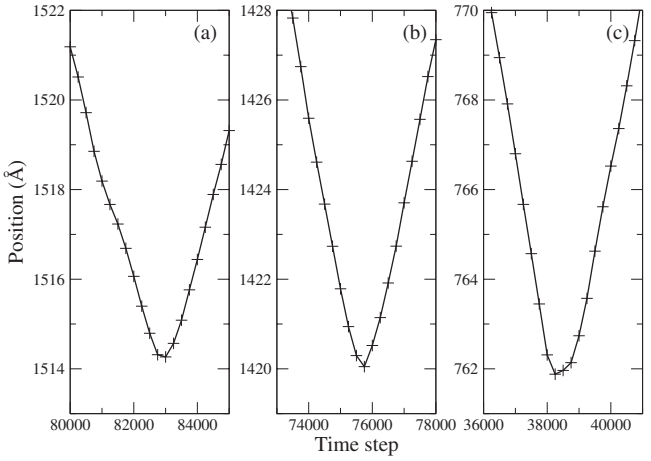

FIG. 3. Plots of the x coordinate of the last molecule as a function of the time step from the NEMD simulations of (a) the long cell, $U_p = 0.63$ km s^{-1}, (b) long cell, $U_p = 1.0$ km s^{-1}, and (c) short cell, $U_p = 1.0$ km s^{-1}.

The starting point for the application of SFABCs is a NEMD simulation of shock loading as described in Sec. II. The shock wave is allowed to propagate until the simulation cell reaches the point of maximum compression. The point of maximum compression can be identified to a high level of accuracy by monitoring as a function of time the x coordinate of the center of mass of the "last" molecule in the simulation cell. The last molecule, the one with the largest x coordinate, can be identified easily by postprocessing analysis of the NEMD simulation. The simulation cells were captured at maximum compression to within a tolerance of 1 Å in the three NEMD simulations described in Sec. II. Plots of the x coordinate of the last molecule as a function of the time step are presented in Fig. 3.

Once the point of maximum compression was identified in the NEMD simulations, the force and velocity vectors of all atoms within the last 30 Å of the cell were set equal to zero. In this manner, those molecules at the end of the simulation cell are treated as a second piston that, together with the first stationary rigid piston, serve to constrain the shock-compressed material at constant volume. In principle, it would also be possible to capture the simulation cell at maximum compression by removing from the system the vacuum region and applying periodic boundary conditions along the shock propagation direction. However, the approach adopted here ensures that the interface between the simulation cell and second piston is structurally coherent, unlike the interface that would be created upon the application of periodic boundary conditions. Furthermore, since the second piston can be made arbitrarily thick, the SFABC method is not affected adversely by the finite width of the shock front.

In the original implementation of the SFABC method,[22] the point of maximum compression was determined by monitoring as a function of time the specific energy content of layers of molecules perpendicular to the direction of shock propagation. The profile of specific energy versus position was fit to a straight line which was extrapolated to predict the time at which the second piston, which is this case was rigid and at rest, was assigned velocity U_p.

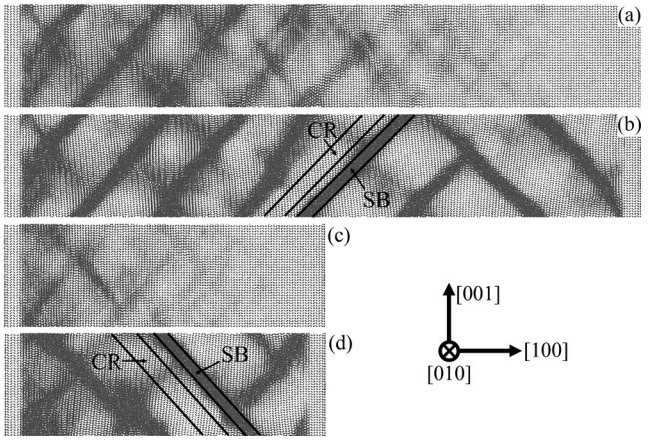

FIG. 4. Projections along [010] of the molecular centers of mass after shock loading at $U_p=1.0$ km s^{-1}. (a) Long cell at maximum compression (Ref. 34), (b) long cell after 121 ps MD simulation under SFABCs (Ref. 34), (c) short cell at maximum compression, and (d) short cell after 110 ps MD simulation under SFABCs. The crystalline regions (CRs) and shear bands (SBs) used for subsequent analysis are indicated in (b) and (d).

IV. RESULTS

A. Shock-induced defects

1. NEMD simulations

The NEMD simulation of the propagation of a planar shock wave along [100] in the long cell at $U_p=0.63$ km s^{-1} ($P_{\mathrm{RH}}=5.7$ GPa) did not result in the nucleation of crystal defects. As noted in Sec. I, at this orientation of the shock propagation direction, none of the dislocation slip systems identified under quasistatic loading conditions[10] are subject to a resolved shear stress.

Shock loading at $U_p=1.0$ km s^{-1} ($P_{\mathrm{RH}}=9.7$ GPa) led to the formation of shear bands during NEMD simulations employing both the long and short cells. Projections of the molecular centers of mass along [010] of the long and short cells at maximum compression are presented in Figs. 4(a) and 4(c), respectively.[35] In both cases, the shock wave propagated from left to right and it is apparent that the shear bands are structurally more developed in the vicinity of the piston since their growth rate is relatively slow compared to the time scale of the simulations. The shear bands propagate at approximately 45° to [100] and the plane of the bands lies in the [010] zone. There appears to be no preference as to whether the shear bands propagate at positive or negative 45° to [100]; the bands are not aligned with any crystallographic orientation of the underlying structure and are driven only by shear stresses which are a maximum at these orientations. However, there is a distinct preference for the plane of the bands to lie in the [010] zone. The shear bands are not appreciably higher in density than the surrounding crystalline regions (CRs); the latter appear to be of low density since in this projection columns of molecules are viewed "end on," while the former comprise amorphous material.

2. SFABC simulations

The SFABC was applied to the simulation cells as described in Sec. III. The long cell shock loaded at $U_p=0.63$ km s^{-1} was simulated in the microcanonical ensemble for 42 ps after the application of SFABCs. The long and short cells shock loaded at $U_p=1.0$ km s^{-1} were simulated in the microcanonical ensemble under SFABCs for 121 and 110 ps, respectively. Snapshots of the long and short cells shock loaded at $U_p=1.0$ km s^{-1} taken at the conclusion of the SFABC simulations are presented in Figs. 4(b) and 4(d), respectively. The SFABCs enable simulation times sufficient for the shear bands to propagate throughout the entire system, and, more importantly, for their internal structure to evolve to a steady-fluctuating state. Detailed analyses of the internal structure of the shear bands are provided in Sec. IV B.

Upon the application of SFABCs, shear bands propagate into the shock-compressed material from the second piston in the opposite orientation to those formed at the first piston. From the moment that the second piston is applied and both ends of the cell are fixed, the total plastic strain mediated by the shear bands in the directions normal to [100] must equal to zero. Hence, growth of the shear bands nucleated in the NEMD simulation is compensated by shear in the opposite sense provided by shear bands growing from the opposite end of the cell. While this may at first seem to be an unphysical artifact associated with SFABCs, it is, in fact, physically correct. We previously observed an abrupt change in the orientation of shear bands in NEMD simulations of systems with very high aspect ratio (15:1 rather than 8:1) owing to the constraints on lateral motion imposed by the unshocked material ahead of the shock front.[36] Hence, in this respect, SFABCs mimic a NEMD simulation using a cell of very high aspect ratio.

Simulations using the long and short cells at $P_{\mathrm{RH}}=9.7$ GPa ($U_p=1$ km s^{-1}) exhibit pronounced finite-size effects whereby one shear band propagates a significant distance through the simulation cell owing to application of periodic boundary conditions. While such finite-size effects are generally undesirable, they in no way affect our conclusions. In Fig. 5 we present a snapshot of the quasi-2D cell after shock loading to 9.7 GPa using NEMD and 56.8 ps of MD simulation after the application of the SFABC. The orientation and dimensions of the quasi-2D cell were selected both to lead to the formation of shear bands (the shortest axis of the cell is parallel to [010]) and to minimize the role of finite-size effects on their subsequent growth. It is clear from Fig. 5 that many shear bands have nucleated randomly both at the pistons and in the bulk. Furthermore, the shear bands have grown at ±45° to [100] in roughly equal amounts. Since only a small fraction of the shear bands cross the (001) periodic boundaries, we propose that the simulated spatial distribution of defects corresponds closely to that which would be observed in a mesoscopic specimen.

B. Structural and thermodynamic analysis

The simulations at $U_p=0.63$ and 1.0 km s^{-1} were examined to quantify shock-induced changes in molecular conformation, the internal structure of the shear bands, and the temperature rise caused by viscous heating during their nucleation and growth. We studied these quantities both for

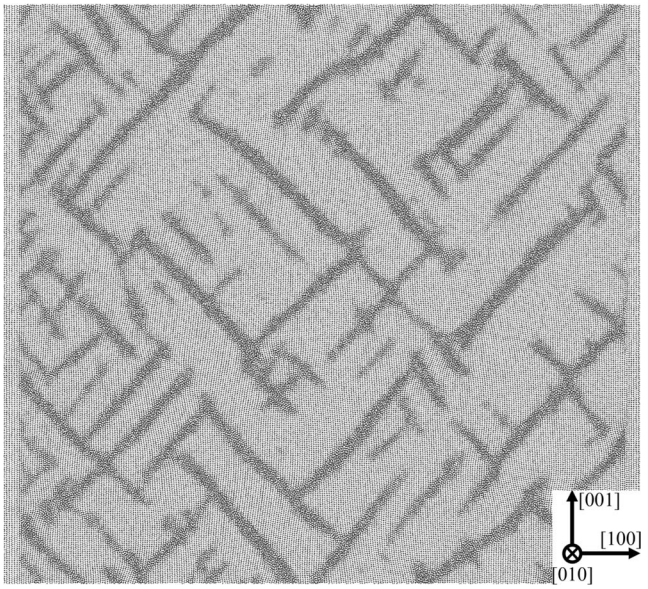

FIG. 5. A projection of the molecular centers of mass of the quasi-2D simulation cell following shock loading to 9.7 GPa using NEMD and a 56.8 ps MD simulation after the application of the SFABC (Ref. 34). At maximum compression, the cell measures $1638.5 \times 34.55 \times 1497.9$ Å^3 parallel to [100], [010], and [001], respectively.

crystalline regions and shear bands adjacent to these regions in our simulations at $U_p = 1.0$ km s^{-1}. The sampled CRs and SBs are indicated in Figs. 4(b) and 4(d).

1. Radial distribution functions

Radial distribution functions (RDFs) for molecular centers of mass were calculated to determine whether the shear bands comprise a liquidlike structure that is consistent with melting and/or amorphization. The RDF is defined as $g(R) = n(R)/4\pi\rho R^2 \Delta R$, where $n(R)$ is the number of particles in a spherical shell of radius R and thickness ΔR and ρ the particle number density. We used $\Delta R = 0.2$ Å in all calculations and ρ was determined uniquely for each system. All RDFs were averaged over at least 7900 molecules.

We plot the RDFs for an unshocked RDX crystal at 300 K and a crystalline region at the point of maximum compression from a NEMD simulation at $U_p = 1.0$ km s^{-1} in Figs. 6(a) and 6(b), respectively. Comparing Figs. 6(a) and 6(b), we find only a small change in the RDFs at first nearest neighbors but notable changes at second-nearest neighbors and beyond. The most relevant feature is the decreased gap between first- and second-nearest neighbors. This is expected due to the large uniaxial compression imparted by shock loading. The RDF of the shock-compressed system becomes relatively smooth at $R > 16$ Å which suggests some loss in long-range order, although the system is still clearly crystalline.

The RDFs calculated for a crystalline region and an adjacent shear band after a 121 ps MD simulation under SFABCs are presented in Figs. 7(a) and 7(b), respectively. The RDF for the crystalline region shows a recovery of the gap between the first- and second-nearest-neighbor shells that was

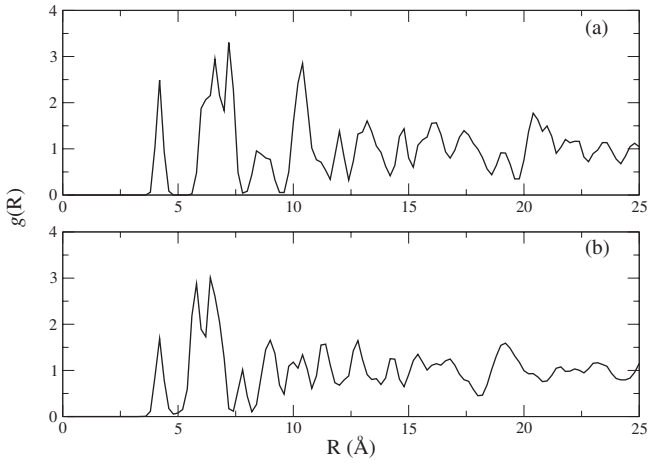

FIG. 6. Center-of-mass radial distribution functions. (a) Unshocked α-RDX crystal at 300 K and (b) crystalline region from the long simulation cell at maximum compression after shock loading at $U_p = 1.0$ km s^{-1}.

reduced during the NEMD phase of the simulation [Fig. 6(b)]. This suggests that SFABCs facilitate the evolution of the system from a metastable configuration after shock loading to geometries more similar to those in the unshocked crystal. The RDF for the shear band corresponds unambiguously to that of a liquidlike state and shows that the shear bands are regions of localized, shear stress-driven amorphization.

2. Heating via viscous flow

The intermolecular and intramolecular temperatures of a crystalline region and adjacent shear band were calculated as a function of time during equilibrium MD simulations employing SFABCs. Plots of the temperatures calculated in the long and short cells are shown in Figs. 8 and 9, respectively. In both the long and short cells, the onset of shear band formation can be discerned clearly by the rapid increase in the intermolecular and intramolecular temperatures that is

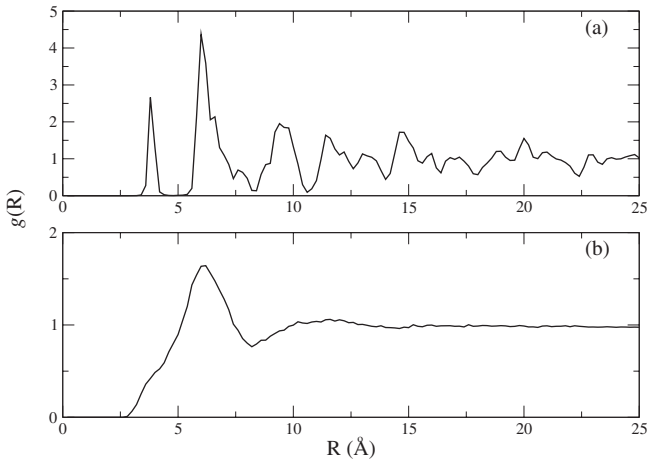

FIG. 7. Center-of-mass radial distribution functions after 121 ps MD simulation under SFABCs. (a) Crystalline region and (b) shear band.

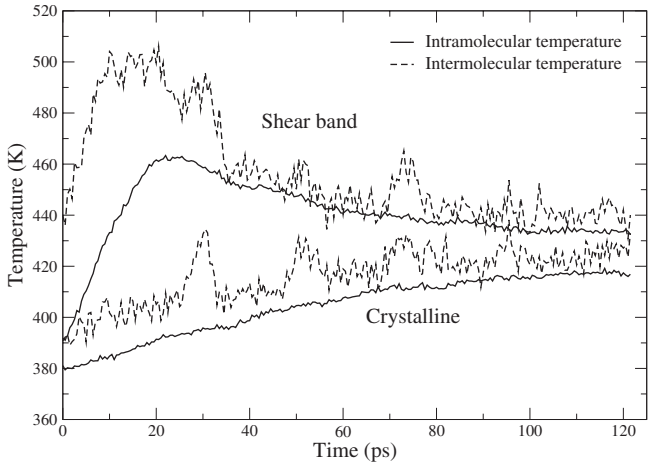

FIG. 8. Intermolecular and intramolecular temperatures of a crystalline region and adjacent shear band during an MD simulation employing SFABCs and the long cell. Zero time corresponds to the start of the SFABC simulation.

driven by viscous flow.[34] In both simulations, the intramolecular temperature within the shear band increases from around 390 to a maximum of 460 K. The passage of the shock wave is responsible for the 90 K increase in intramolecular temperature compared to that in the unshocked RDX crystal. The heating rate within the shear band is about 3.5×10^{12} K s^{-1} during the initial stage of growth in the long cell and about 5.8×10^{12} K s^{-1} in the short cell.

The intense direct heating of material in the shear bands during viscous flow drives the indirect heating of the surrounding crystalline regions. After the initial growth of the shear bands, the intermolecular and intramolecular temperatures equilibrate throughout the crystal. Both simulations suggest that temperatures of the shear bands and bulk will equilibrate to about 430 K. Here we are using a nonreactive potential, but in reality the intense heating and viscous flow associated with the formation of shear bands would cause some RDX molecules to decompose via a strongly exothermic path. Assuming that this chemistry progresses to the exothermic steps in the decomposition mechanism, the heating would be enhanced by the processes. Nevertheless, the release of stored elastic strain energy that the formation of shear bands facilitates increases the temperature of the entire crystal by 40–50 K over that due to the passage of the shock wave alone.

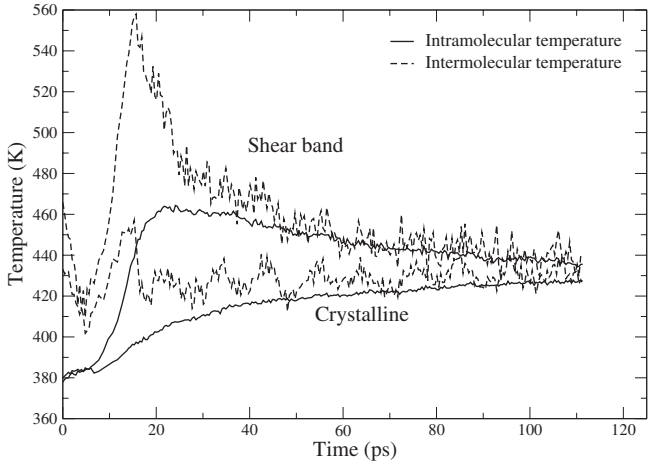

FIG. 9. Intermolecular and intramolecular temperatures of a crystalline region and adjacent shear band during an MD simulation employing SFABCs and the short cell. Zero time corresponds to the start of the SFABC simulation.

It is important to note that the levels of shock heating we calculate from our classical MD simulations underestimate those that would take place in a real organic molecular crystal. Within classical MD, each degree of vibrational freedom is associated with a thermal energy $k_B T/2$. However, the Debye temperatures of the intramolecular vibrational modes in RDX are known to be significantly higher than room temperature (see, for example, Ref. 37). Thus, the true heat capacity of RDX under ambient conditions is significantly less than the classical limit.

The shock compression determined from our NEMD simulations of shock loading to $P_{\mathrm{RH}}=9.7$ GPa is $V/V_0=0.82$. This can be considered a weak shock since P_{RH} is less than the bulk modulus of the material. Using experimental and experimentally derived values for material properties, we can estimate the shock heating that takes place in real RDX under the same loading conditions by summing contributions from the heating upon isentropic compression from specific volume V_0 to V, ΔT_S, and from the additional heating that arises from the passage of the shock front, ΔT_H, i.e.,[37]

$$\Delta T = \Delta T_S + \Delta T_H, \tag{1}$$

where

$$\Delta T_S = T_0 \left[\exp\left(- \int_{V_0}^{V} \frac{\Gamma}{V} dV \right) - 1 \right] \tag{2}$$

and

$$\Delta T_H = \int_{e_S(V)}^{e_H} \frac{de}{c_v}. \tag{3}$$

Here, Γ is the Grüneisen coefficient, T_0 the initial temperature, c_v the heat capacity at constant volume, $e_S(V)$ the specific energy on the initial isentrope, and e_H the specific energy on the Hugoniot. We calculated $c_v=1077.0$ J kg^{-1} K^{-1} and $\Gamma=1.103$ using published room-temperature values for the heat capacity at constant pressure, c_p,[30] the coefficient of volumetric thermal expansion,[38] isentropic bulk modulus, K_S,[28] and ideal equilibrium density, ρ_0.[12] These values yield $\Delta T_S=74$ K. The pressure on the isentrope expanded to leading order about the equilibrium specific volume, V_0, is

$$P_S(V) = K_S \left[\left(1 - \frac{V}{V_0} \right) + \mathcal{G} \left(\frac{V}{V_0} - 1 \right)^2 \right], \tag{4}$$

where $\mathcal{G}$ is the fundamental derivative.[39] The energy on the initial isentrope can be expressed analytically as

$$e_S(V) = -\int_{V_0}^{V} P_S(V)dV, \tag{5}$$

$$= \frac{K_S}{\rho_0}\left\{(1+\mathcal{G})\left(1-\frac{V}{V_0}\right) - \left(\mathcal{G}+\frac{1}{2}\right)\left[1-\left(\frac{V}{V_0}\right)^2\right] + \frac{\mathcal{G}}{3}\left[1-\left(\frac{V}{V_0}\right)^3\right]\right\}. \tag{6}$$

An experimental value for fundamental derivative was obtained from the gradient of the Hugoniot in the $U_s - U_p$ plane determined from isentropic compression experiments on RDX (100), namely, $\mathcal{G}=5.6$.[39,40] The energy on the Hugoniot is given simply by the Hugoniot equation,[21,39]

$$e_H = \frac{P_{\mathrm{RH}}}{2\rho_0}\left(1-\frac{V}{V_0}\right). \tag{7}$$

Combining the values of P_{RH} and V/V_0 from our NEMD simulations and the calculated values of $e_S(V)$, e_H, and c_v with Eq. (3), we estimate the additional heating arising only from the passage of the shock front, $\Delta T_H = 289$ K. Hence, the total temperature increase in real RDX during shock loading is about $\Delta T = 363$ K. Thus, our classical MD simulations underestimate the true shock heating by factor of about 4, although this should be considered to be an upper limit owing to the temperature dependence of the experimental heat capacities and Γ.

3. Rotational order

A rotational order parameter, P_2, was used to determine the onset of shear band formation and characterize their internal structure. P_2 characterizes the relative orientation between a given vector within each molecule, in this case the vector connecting carbon and nitrogen atoms on opposite sides of the six-membered ring, at time $t=0$ and that same vector at subsequent time. P_2 is defined as

$$P_2(t) = \frac{1}{N}\sum_{i=1}^{N}\frac{1}{2}[3(\hat{\mathbf{n}}_i(0)\cdot\hat{\mathbf{n}}_i(t))^2 - 1], \tag{8}$$

where N is the number of molecules and $\hat{\mathbf{n}}_i(t)$ the unit vector between specified atoms in molecule i at time t and P_2 equals unity in a system with perfect rotational order and $1/4$ when there is no rotational order.

Plots of P_2 for a crystalline region and an adjacent shear band in the long and short cells shock loaded at $U_p = 1.0$ km s^{-1} are shown in Figs. 10(a) and 10(b), respectively. The rotational order parameters calculated during the NEMD and SFABC simulations have been merged so that they are plotted as a function of the total simulation time. All plots are continuous in value and gradient across the vertical lines which denote the time at which the SFABC was applied, providing convincing evidence that applying SFABCs, in this case, does not introduce unphysical artifacts in the simulations.

Owing to thermal motion, $P_2 \approx 0.96$ in the perfect crystal at 300 K. We do not observe a significant change in the value of P_2 after the passage of a shock wave although Fig. 7 shows notable differences in the RDFs of the shocked and unshocked systems. Hence, shock loading changes significantly the crystal structure on a center-of-mass level but individual molecules largely retain their original orientation.

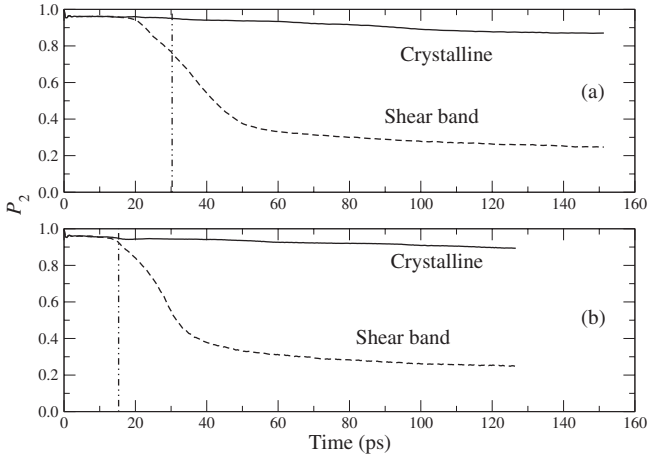

FIG. 10. Rotational order parameter in a crystalline region and shear band after shock loading at $U_p = 1.0$ km s^{-1}. The vertical line denotes the time at which SFABCs were applied. (a) Long cell and (b) short cell.

The rotational order parameter reveals clearly the onset of shear band formation and its subsequent structural evolution. In both the long and short cells, P_2 decreases rapidly from about 0.96 to about 0.35 during the initial stage of growth where the rate of viscous heating is high and amorphization progresses rapidly. The initial stage of growth takes about 20–30 ps. The shear bands subsequently evolve relatively slowly to a state of rotational disorder over a time period of about 100 ps. This secondary stage of growth is associated with the equilibration of the thermal gradients generated during the initial growth stage, as described in Sec. IV B 2. The rotational order parameter for the crystalline regions decreases slowly during shear band formation from about 0.96 to about 0.88. We attribute this decrease to both the 40–50 K rise in temperature in the crystalline regions that results from the intense heating in the shear bands and the misorientation of the crystalline regions with respect to their original axes due to the shear strains mediated by viscous flow (see Fig. 4).

We computed the autocorrelation function, averaged over all time origins, of the rotational order parameter for eight representative molecules randomly dispersed within a shear band. By fitting the initial decay of the autocorrelation function to $C(t) = A\exp(-t/\tau)$, where A is a constant, we estimate that the molecules within the shear bands lose memory of their initial orientation and amorphize within a characteristic time interval of $\tau^* = 9.7$ ps.

4. Molecular conformation

At ambient temperature and pressure, the point group of molecules in the α-RDX crystal structure is C_s. The six-membered ring is in a chair conformation with two nitramine group N-N bonds oriented axially (A) to the ring and one equatorially (E); this molecular conformation is commonly

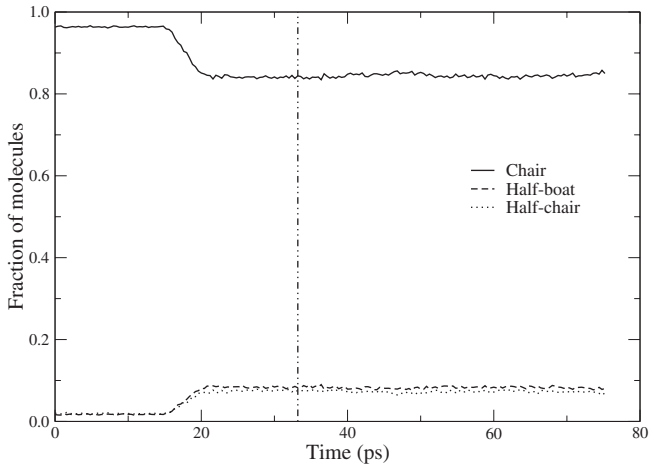

FIG. 11. Fraction of molecules in a given ring conformation after shock loading at $U_p=0.63$ km s^{-1}. The vertical line denotes the time at which SFABCs were applied.

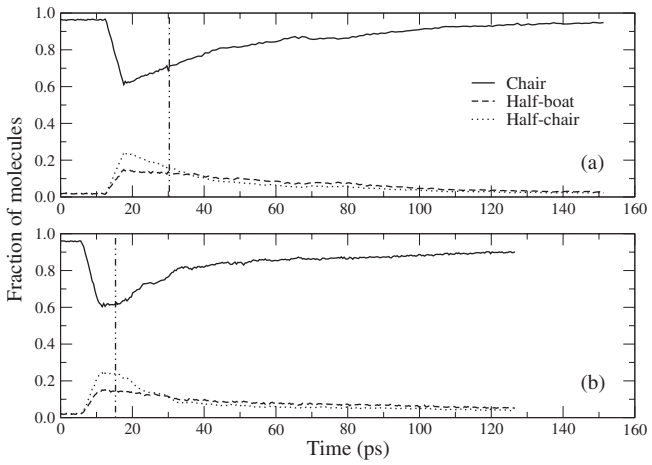

FIG. 12. Fraction of molecules in a given ring conformation in a crystalline region after shock loading at $U_p=1.0$ km s^{-1}. The vertical lines denote the time at which SFABCs were applied. (a) Long cell and (b) short cell.

denoted as *AAE*. Shock compression or melting/amorphization may change the ring conformation and/or the orientations of the three nitro groups with respect to the ring. To characterize the geometry of the molecular ring we calculated ring-puckering coordinates using the formalism of Cremer and Pople.[41] The orientation of the three nitro groups with respect to the ring was determined by calculating the angles between the three N-N bonds and the vector normal to the ring.

In Fig. 11 we plot the fraction of molecules in a given ring conformation as a function of the total NEMD plus SFABC simulation time during shock loading at $U_p=0.63$ km s^{-1} ($P_{\mathrm{RH}}=5.7$ GPa). Before the arrival of the shock wave in the examined region of the simulation cell, 96% of the molecular rings are in the chair conformation and 2% are in each of the half-boat and half-chair conformations. The passage of the shock wave through the sampled volume induces a change in the relative populations of the three conformations, namely, the fraction of molecular rings identified as being in the chair conformation falls to 85%, while those in the half-boat and half-chair conformations increase to 8% and 7% of the total, respectively. The fraction of molecular rings in the boat and twist-boat conformations is negligible both before and after the passage of the shock front. Furthermore, we did not detect nitro-group conformations other than *AAE*. Since no deformation mechanisms are active to relieve the uniaxial shock compression at this U_p, the relative populations of molecules in these three ring conformations remain constant.

The same analysis was performed for a crystalline region and adjacent shear band in the long and short cells shock loaded at $U_p=1.0$ km s^{-1}. The fractions of molecules in a given ring conformation as a function of total simulation time in crystalline regions in the long and short cells are plotted in Figs. 12(a) and 12(b), respectively. Behavior similar to that observed under shock loading at $U_p=0.63$ km s^{-1} was found but with some important differences. First, the passage of the shock front through the sampled regions mediates a greater shift in the relative populations of the ring conformations. In both the long and short simulation cells, immediately after the passage of the shock front, only 60% of the molecular rings are identified as chair conformers. The fractions of half-boat and half-chair conformations do not increase in equal amounts; initially 25% of molecules adopt the half-chair conformation and 15% the half-boat conformation. As before, in the crystalline regions we observe negligible fractions of the boat or twist-boat conformations or nitro groups in orientations other than *AAE*. However, since in these simulations at $U_p=1.0$ km s^{-1} shear bands form that relax the large shock-induced shear stresses, the crystalline regions are able to relax to a state in which the average molecular conformation is more similar to that in a perfect α-RDX crystal. Hence, as shear bands grow throughout the system, the fraction of molecular rings identified as being in the chair conformation in the crystalline regions increases to around 90% over 100 ps, while the fraction of molecular rings in the half-boat and half-chair conformations decay accordingly. Thus, we propose that plastic deformation via the formation and growth of shear bands under shock loading in (100)-oriented RDX single crystals is largely driven by the free energy released upon relaxation of the shock-induced ring conformations to relative populations that are more consistent with the α-RDX crystal structure.

Analyses of molecular ring conformations in the shear bands in the long and short cells are presented in Figs. 13(a) and 13(b), respectively. As for the crystalline regions, immediately following the passage of the shock front around 60% of molecular rings are in the chair conformation with 25% and 15% in the half-chair and half-boat conformations, respectively. These populations begin to relax initially due to the growth of shear bands elsewhere in the cells. However, once shear bands start to propagate into these volumes and melting commences, the populations of the five possible ring conformations evolve to distributions more consistent with the liquid state. In both the long and short cells, the fractions of molecular rings in the chair, half-boat, and half-chair conformations decrease over 100 ps to 34%, 13%, and 12%, respectively. In contrast to the crystalline regions discussed in the preceding paragraph, 20% and 21% of the molecular rings in the shear bands are in the boat and twist-boat con-

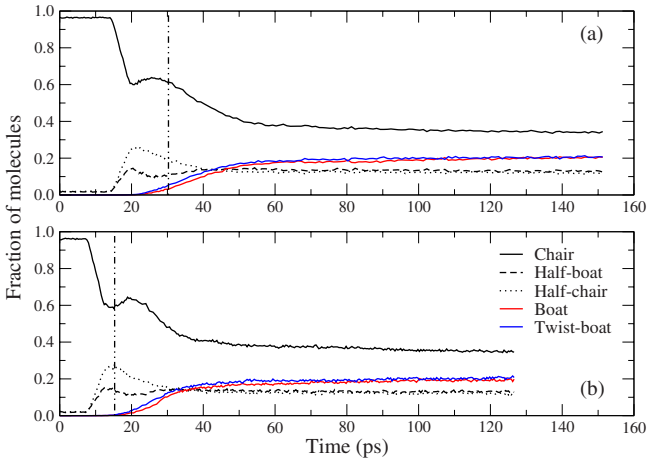

FIG. 13. (Color online) Fraction of molecules in a given ring conformation in a shear band after shock loading at $U_p = 1.0$ km s^{-1}. The vertical lines denote the time at which SFABCs were applied. (a) Long cell and (b) short cell.

formations, respectively. Hence, the appearance of molecules in these conformations signals the onset of melting since they serve as an indicator of the increase in conformational disorder facilitated by the liquid state. Furthermore, at the same simulation times that increase in the populations of boat and twist-boat conformations are observed, we also find notable increases in the fraction of molecules identified as not being in the *AAE* conformation. The fractions of molecules within the shear bands in the long and short simulation cells identified as not possessing the *AAE* conformation—that is, those molecules whose nitro groups are in an *AEE* or *EEE* conformation—are plotted as a function of total simulation time in Figs. 14(a) and 14(b), respectively. In both the long and short cells, around 30% of the molecules in the shear bands are not in the *AAE* conformation once a steady-fluctuating state is achieved. Although the *AAA* conformation is suggested to be favored in the gas phase,[42,43] we detect only a negligible number of molecules in this conformation in the condensed phase.

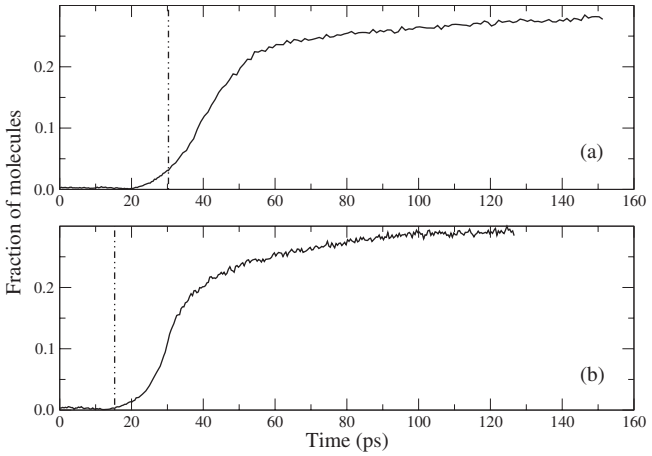

FIG. 14. Fraction of molecules in a shear band with nitro groups not in the *AAE* conformation after shock loading at $U_p = 1.0$ km s^{-1}. The vertical lines denote the time at which SFABCs were applied. (a) Long cell and (b) short cell.

V. DISCUSSION AND CONCLUSIONS

A. Efficacy of the SFABC method

The use of SFABCs allowed us to extend simulation times to the extent that shock-induced shear bands, which evolve slowly on the time scale of a typical NEMD simulation, could be studied over their complete evolution to a steady-fluctuating state. This is demonstrated with greatest clarity in Figs. 13 and 14 where relative abundances of the ring and nitro-group conformations at the point of maximum compression in the respective NEMD simulations, as denoted by the vertical broken lines, differ significantly from those once a steady state is reached. More generally, the absence in Figs. 10–14 of perturbations associated with the application of the SFABC at the moment of maximum compression further supports the validity of the approach.

There are certain situations where the application of SFABCs may not be appropriate. For example, it would be difficult to apply this method in the study of shock waves in ductile metals where, in the two-wave regime, an elastic precursor may lead a strong plastic wave by tens of nanometers. In this case, if SFABCs are applied when the elastic precursor reaches the free surface, the slower plastic wave may reflect off the second piston, setting up undesirable density waves in the material. However, this problem could be overcome within the SFABC framework by applying the second piston within the simulation cell at a point that has been passed by both the elastic and plastic waves rather than at the end of simulation cell. This approach would still require a computationally expensive NEMD simulation, but subsequent MD simulations could be performed using a smaller number of atoms. In the case of shock waves in RDX, we do not find strong plastic waves that lag significantly behind the elastic precursor; hence the SFABC method is particularly adept at capturing the simulation cell at maximum compression.

Hugoniostat methods have been developed that allow shock loading to be simulated within the framework of MD and which are less computationally demanding than large-scale NEMD simulations.[19,44–47] These methods modify the equation of motions of atoms to drive a system toward a prescribed state on the Hugoniot locus. It is not obvious that Hugoniostats are appropriate tools for use in the simulation of molecular crystals since phenomena at the shock front in these materials are extremely complex owing to their relatively low symmetry and many intramolecular degrees of freedom. Explicit simulation of the shock front using NEMD will provide a more accurate description of, for example, the initial overshoot in intermolecular temperature and its equilibration with the intramolecular vibrational modes in the nanometers behind the shock front.[14,27] Previous work showed that these phenomena are of fundamental importance to the homogeneous nucleation of dislocations in (111)-oriented RDX single crystals.[14] However, Hugoniostats do provide certain advantages over SFABCs; for example, the former ensures that the system remains on the Hugoniot locus, while the latter, in general, does not. SFABCs capture the simulation cell at a constant volume that corresponds only to the system after the passage of the leading shock wave(s).

Shock-induced phase transformations or plastic deformation that lags the elastic wave will reduce the diagonal component of the stress tensor parallel to the direction of shock propagation and the system under SFABCs will depart from the Hugoniot locus. Hugoniostat methods enforce a constant pressure rather than a constant volume simulation. This limitation of the SFABC method may be acceptable in certain circumstances, for example, if one wishes to extend simulation times to identify events that occur at a rate too low to be observed directly in NEMD simulations, such as the homogeneous nucleation of dislocations, second phases, or the initiation of slow, complex chemical reactions. Hence, the SFABC method may be of particular advantage in cases where the description of interatomic bonding is sufficiently expensive that large-scale NEMD simulations are not feasible but an accurate treatment of the dynamics associated with the shock front is required. The principal advantages of SFABCs over Hugoniostats are that the former are extremely simple to implement, robust, do not affect the equations of motion of atoms artificially, and provide an essentially exact treatment of phenomena at the shock front.

In order to reach the same total NEMD plus SFABC simulation time for the material subvolumes sampled here in a normal NEMD simulation, a simulation cell of length $604a$, containing over 40×10^6 atoms, would be required. Such simulations would be computationally challenging at present (the simulation reported here using the quasi-2D cell required 8.8 CPU years). Thus, the SFABC method facilitates simulations that otherwise may be prohibitively expensive. Furthermore, the results reported in Sec. IV B for the long and short cells, the latter containing half the number of atoms of the former, concur in every regard once a steady-fluctuating state is achieved (these simulations appear to differ only in the rate of shear band formation). Thus, SFABCs not only enable simulation times to be extended for a given cell size but also facilitate simulations with significantly fewer atoms with no loss in the accuracy of the description of the final state. Finally, in comparison with Hugoniostat methods, use of the SFABC provides an exact treatment of the dynamics during shock loading and is far more simple and robust in its implementation.

B. Implications for initiation sensitivity

Dislocation-mediated plasticity was not observed during shock loading at either $U_p=0.63$ km s^{-1} ($P_{\mathrm{RH}}=5.7$ GPa) or $U_p=1.0$ km s^{-1} ($P_{\mathrm{RH}}=9.7$ GPa). This result was expected for this orientation of the shock propagation direction since none of the slip systems identified under quasistatic loading are subject to a resolved shear stress.[13] Furthermore, we can eliminate the possibility that for this orientation of the shock propagation direction, other previously unknown slip systems are activated by the passage of the shock wave; that is, phenomena such as those observed during shock loading on (111) (Ref. 14) do not occur for this orientation. Thus, based on the steric-hindrance model, we expect high sensitivity for impacts on (100), in accord with Ref. 13.

An unanticipated deformation mechanism was identified during shock loading on (100) at $U_p=1.0$ km s^{-1}, namely, the formation and growth of shear bands. While the steric-hindrance model suggests that deformation mechanisms which serve to relax shear stresses promote low impact sensitivity, the intense heating caused by viscous flow within the shear bands will certainly promote thermal molecular decomposition. Moreover, viscous flow may promote the mechanical rupture of intramolecular bonds, further enhancing the rate of molecular decomposition. Thus, in a sense, shear bands can be considered to be homogeneously nucleated hot spots since the potential energy stored in the shock compressed material is partly released in spatially localized material subvolumes.

One might expect that if dislocation slip systems could be activated at relatively low values of P_{RH} at this orientation of the shock propagation direction, then shear stresses would not build to the level where deformation via shear bands is inevitable. However, NEMD studies of shock waves in α-HMX by Jaramillo *et al.*[27] revealed a gradual transition from dislocation-mediated plasticity to deformation mediated by the growth of liquidlike shear bands with increasing P_{RH}. Hence, the deformation of energetic molecular crystals via the nucleation and growth of shear bands appears to be related to intrinsic instabilities of the crystal structure.

C. Comments on the effects of nonclassical phenomena in simulations of nonequilibrium processes in molecular crystals

It is well known that in the temperature range of interest in this study, the heat capacity of a system of classical oscillators with a frequency distribution representative of a molecular crystal is significantly larger than the value in the corresponding quantum-mechanical system; thus, for the weak-to-moderate shock strengths considered here, the shock temperature predicted on the basis of classical MD will be lower than the "real" value, as was shown in Sec. IV B 2. Nevertheless, this underestimate, which is inherent to the use of classical mechanics, does not affect our underlying theses, namely, that the homogeneous nucleation of liquidlike shear bands occurs in [100]-oriented RDX crystals under sufficiently strong shock loading and the viscous flow of material within these defects leads to an *additional*, non-negligible localized heating. Since our simulations underestimate the magnitude of the shock heating, it is a reasonable assumption that experimentally these defects will nucleate at significantly lower shock pressures. Furthermore, the magnitude of the heating in the shear bands will be higher than the 70–90 K we calculate since the "error" in the heat capacity of material due to classical mechanics is equally present within these subvolumes. Thus, while our calculated shock and defect temperatures are low compared to those in real, quantum dynamical RDX, they are almost directly proportional; that is, based on specific heat alone, classical MD simulations will also underestimate the additional heating within the shear bands by roughly the same factor of 4 as was predicted for the shock heating.

Fundamentally, the "specific-heat problem" of interest here for the case of a condensed phase molecular system and the "zero-point energy problem" that arises for the case of

gas-phase polyatomic molecules are manifestations of quantum effects and have no classical analog. At present there is no satisfactory method for performing large-scale MD simulations with a quantum-mechanically accurate treatment of the zero-point energy problem (for gas-phase species) or the specific-heat problem (for condensed molecular phases). Nevertheless, our simulations were designed to mitigate in a physically sensible way the overestimation error in the specific heat of RDX by freezing out via geometric constraints, the contributions to the heat capacity from vibronic degrees of freedom with the highest modal Debye temperature, namely, the C-H bond stretches. Attempts to go beyond this type of strategy are problematic: Thompson and co-workers[48,49] demonstrated that for model Hamiltonians with small numbers of degrees of freedom that both "active" and "passive," quantum-inspired corrections to classical dynamic trajectories may result in severely unphysical behavior. Specifically, even for systems containing only zero-point vibrational energy, observables obtained from uncorrected classical MD trajectories resembled more closely the true quantum-mechanical ones than those obtained for trajectories that included quantum-corrected classical dynamics.

Another option, essentially a generalization of the idea of freezing out the high-frequency degrees of freedom employed in the current study, is to introduce a Debye-type dependence of the heat capacity on temperature using the mesoparticle dynamics of Strachan and Holian.[50] In this approach, a reduced-dimension representation of the potential-energy function results in a significant decrease in the classical heat capacity of the system. This is balanced by introducing into the equations of motion for the system "implicit degrees of freedom" that correspond to local heat reservoirs within the mesoparticles. These internal degrees of freedom can be populated using either classical or quantum statistical descriptions of their behavior. While this approach is attractive, it is rather empirical and mesopotentials presently do not demonstrate the levels of sophistication needed to describe accurately a system as complex as an RDX crystal under extreme loading conditions. Thus, although simulations based on classical MD display certain well-known and well-understood limitations, at present there exists no better tool for the study of shock-induced phenomena in organic molecular crystals.

ACKNOWLEDGMENTS

M.J.C. and T.D.S. thank Eugenio Jaramillo for assistance with LAMMPS and Sam Shaw, Ralph Menikoff, Dan Hooks, and Kyle Ramos for many fruitful discussions. L.Z. is grateful for Wei Yang's support. This work was supported by the National Nuclear Security Administration of the U.S. Department of Energy under Contract No. DE-AC52-06NA25396 with Los Alamos National Security, LLC (M.J.C. and T.D.S.) and a U.S. Department of Defense MURI grant managed by the Army Research Office (L.Z. and D.L.T.).

APPENDIX: CONSERVATION OF ENERGY IN SFABC SIMULATIONS

As discussed briefly in Sec. I, shock waves can be generated in NEMD simulations by driving a piston at a specified U_p into a stationary simulation cell as in Ref. 22 or by impacting a simulation cell onto a fixed rigid piston at a specified U_p. For convenience and clarity, we refer hereafter to these approaches as the moving-piston and moving-cell methods, respectively. These methods are Galilean invariant, thus it is largely a matter of personal preference which is employed. However, we found unexpected differences between these formally equivalent methods upon the application of SFABCs.

If the moving-piston method is used to generate the shock wave in a NEMD simulation, SFABCs can be applied in much the same way as described in Sec. III. The time at which the simulation cell reaches maximum compression can be determined with high accuracy by again plotting as a function of time the x coordinate of the center of mass of the last molecule and identifying when the curvature becomes nonzero. The second piston is then applied by setting the force and velocity vectors of all atoms within a specified distance from the end cell to zero and $(U_p,0,0)$, respectively. In this manner, the volume of the cell is fixed to that corresponding to maximum compression and the entire system translates with a velocity $(U_p,0,0)$.

When a shock wave was generated in (100)-oriented RDX using the moving-cell method at $U_p=1.0$ km s^{-1} and SFABCs were applied as in Sec. III, during equilibrium MD simulations in the microcanonical ensemble, total energy was conserved to a tolerance of 1.2 ppm. However, when the moving-piston method was employed we found that the total energy was conserved to only 2.2 parts per thousand using otherwise identical computational protocols. Despite the thousandfold decrease in energy conservation in the latter simulation, we found that the relative particle trajectories in the two simulations were identical until numerical divergences arose due to chaotic dynamics.

The origin of the apparent poor conservation of the total energy when the simulation cell translates is determined entirely by the contribution from the kinetic energy, T, to the total energy. We can write the kinetic energy of an ensemble of N thermalized particles of mass m_i in a system whose center of mass translates with constant velocity $\mathbf{U}=(U_p,0,0)$ as

$$T(\mathbf{U}) = \frac{1}{2}\sum_{i=1}^{N}\left[m_i\mathbf{v}_i\cdot\mathbf{v}_i + m_i\mathbf{U}\cdot\mathbf{U} + 2m_i\mathbf{v}_i\cdot\mathbf{U}\right], \quad \text{(A1)}$$

where $\mathbf{v}_i=(v_i^x,v_i^y,v_i^z)$ is the velocity of particles with respect a coordinate system translating with velocity $\mathbf{U}$. The first term is related to the temperature of the ensemble and the second term is a constant. The third term, T', is a contribution to the kinetic energy arising from the momentum of the system parallel to $\mathbf{U}$,

$$T' = U_p\sum_{i=1}^{N} m_i v_i^x. \quad \text{(A2)}$$

Hence, the apparent poor conservation of the total energy of simulation cells under SFABCs translating with velocity U_p is explained by fluctuations of the total momentum, $\Sigma_{i=1}^{N} m_i v_i^x$. Hence, in the microcanonical ensemble, MD configuration

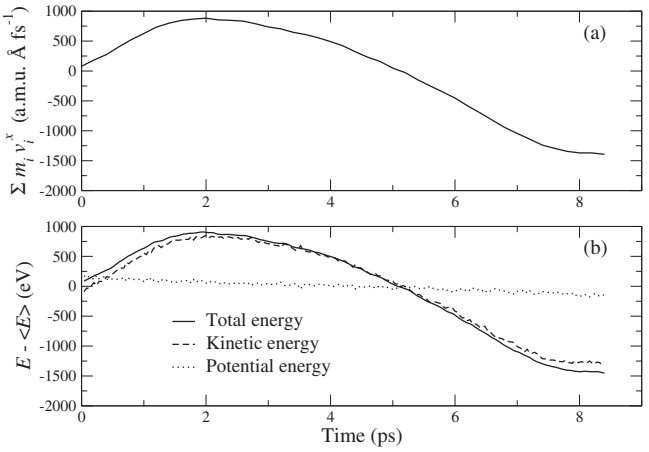

FIG. 15. (a) Oscillation of the total momentum in a system under SFABCs translating with velocity at $U_p=1.0$ km s^{-1} and (b) deviations of the total, kinetic, and potential energies of the system from their mean values.

trajectories are independent of **U** (i.e., they are Galilean invariant in configuration space), but the kinetic energy of the system depends on the scalar product of the total momentum with **U**.

To illustrate the contribution from the nonconserved linear momentum to the kinetic energy in a translating system we plot in Fig. 15(a) the quantity $\Sigma_{i=1}^{N} m_i v_i^x$ as a function of simulation time for an RDX crystal under SFABCs. The simulation cell was shock loaded using the moving-piston method and is translating with velocity $U_p=1.0$ km s^{-1}. In Fig. 15(b) we plot as a function of simulation time the deviation of the total, kinetic, and potential energies of the system from their mean values time averaged over the simulation. Comparing Figs. 15(a) and 15(b) it is evident that the kinetic and total energies track oscillations of the total momentum, while the potential energy, which reflects the relative particle trajectories of the system, is independent of the total momentum. The slow decrease in the potential energy in Fig. 15(b) arises from the nucleation and growth of shear bands in the system.

*cawkwell@lanl.gov
†sewell@lanl.gov
‡Present address: School of Computational Science, Florida State University, Tallahassee, Florida 32306, USA.
§thompsondon@missouri.edu

[1] A. E. D. M. van der Heijden, R. H. B. Bouma, and A. C. van der Steen, Propellants, Explos., Pyrotech. **29**, 304 (2004).
[2] R. Menikoff, in *Shock Compression of Condensed Matter—2003*, edited by M. D. Furnish, Y. M. Gupta, and J. W. Forbes (American Institute of Physics, Melville, NY, 2004), p. 393.
[3] S. M. Chitanvis, *Shock Compression of Condensed Matter—2003* (Ref. 2), p. 319.
[4] H. W. Sandusky, B. C. Glancy, D. W. Carlson, W. L. Elban, and R. W. Armstrong, J. Propul. Power **7**, 518 (1991).
[5] J. K. Dienes, Q. H. Zuo, and J. D. Kershner, J. Mech. Phys. Solids **54**, 1237 (2006).
[6] T. Boddington, P. Gray, and G. C. Wake, Proc. R. Soc. London, Ser. A **357**, 403 (1977).
[7] J. J. Dick, Appl. Phys. Lett. **44**, 859 (1984).
[8] J. J. Dick, R. N. Mulford, W. J. Spencer, D. R. Pettit, E. Garcia, and D. C. Shaw, J. Appl. Phys. **70**, 3572 (1991).
[9] J. J. Dick, J. Appl. Phys. **81**, 601 (1997).
[10] H. G. Gallagher, P. J. Halfpenny, J. C. Miller, and J. N. Sherwood, Philos. Trans. R. Soc. London **339**, 293 (1992).
[11] J. J. Dick and J. P. Ritchie, J. Appl. Phys. **76**, 2726 (1994).
[12] C. S. Choi and E. Prince, Acta Crystallogr., Sect. B: Struct. Crystallogr. Cryst. Chem. **28**, 2857 (1972).
[13] D. E. Hooks, K. J. Ramos, and A. R. Martinez, J. Appl. Phys. **100**, 024908 (2006).
[14] M. J. Cawkwell, T. D. Sewell, K. J. Ramos, and D. E. Hooks (unpublished).
[15] All of the simulations described in this work were performed in the microcanonical (*NVE*) ensemble using Newton's equations without modification or coupling to external fields. In order to maintain consistency with the prior literature on molecular dynamics simulations of shock waves, we use the nomenclature "NEMD" nonequilibrium molecular dynamics to describe the microcanonical evolution of a system of particles with a highly nonequilibrium distribution of momenta at the beginning of the simulation. This use of NEMD should not be confused with explicitly non-Newtonian methods used by others; See, for example, S. S. Sarman, D. J. Evans, and P. T. Cummings, Phys. Rep. **305**, 1 (1998).
[16] B. L. Holian and P. S. Lomdahl, Science **280**, 2085 (1998).
[17] B. L. Holian, Shock Waves **5**, 149 (1995).
[18] B. L. Holian, Shock Waves **13**, 489 (2004).
[19] F. Barmes, L. Soulard, and M. Mareschal, Phys. Rev. B **73**, 224108 (2006).
[20] E. M. Bringa, A. Caro, M. Victoria, and N. Park, JOM **57**, 67 (2005).
[21] Y. B. Zel'dovich and Y. P. Raizer, *Physics of Shock Waves and High-Temperature Hydrodynamic Phenomena* (Academic, San Diego, 1966), Vol. I.
[22] A. V. Bolesta, L. Zheng, D. L. Thompson, and T. D. Sewell, Phys. Rev. B **76**, 224108 (2007).
[23] In order to distinguish our method for absorbing the shock front in molecular dynamics simulations from the extensive literature on absorbing boundary condition (ABC) methods for acoustic waves, we hereafter refer to the approach first described by Bolesta *et al.* (Ref. 22) as the shock-front absorbing boundary condition method (SFABC).
[24] S. Namilae, D. M. Nicholson, P. K. V. V. Nukala, C. Y. Gao, Y. N. Osetsky, and D. J. Keffer, Phys. Rev. B **76**, 144111 (2007).
[25] G. D. Smith and R. K. Bharadwaj, J. Phys. Chem. B **103**, 3570 (1999).
[26] D. Bedrov, C. Ayyagari, G. D. Smith, T. D. Sewell, R. Menikoff, and J. M. Zaug, J. Comput.-Aided Mater. Des. **8**, 77 (2001).
[27] E. Jaramillo, T. D. Sewell, and A. Strachan, Phys. Rev. B **76**, 064112 (2007).
[28] R. B. Schwarz, D. E. Hooks, J. J. Dick, J. I. Archuleta, and A. R.

Martinez, J. Appl. Phys. **98**, 056106 (2005).
[29] *LASL Explosive Property Data*, edited by T. R. Gibbs and A. Popolato (University of California, Berkeley, 1980).
[30] B. Olinger, B. Roof, and H. Cady, *Comportement des Milieux Denses sous Hautes Pressions Dynamiques* (Commissariat à l'Energie Atomique, Paris, 1978), p. 4.
[31] E. Jaramillo and T. D. Sewell (unpublished).
[32] S. J. Plimpton, J. Comput. Phys. **117**, 1 (1995).
[33] S. J. Plimpton, R. Pollack, and M. Stevens, Proceedings of the Eighth SIAM Conference on Parallel Processing for Scientific Computing (SIAM, Philadelphia, 1997).
[34] See EPAPS Document No. E-PRBMDO-78-060825 for movies of the formation of shear bands under shock loading to 9.7 GPa and their evolution upon the application of the SFABC. For more information on EPAPS, see http://www.aip.org/pubservs/epaps.html.
[35] Figures 4 and 5 were rendered using the AtomEye atomistic configuration viewer: J. Li, Modell. Simul. Mater. Sci. Eng. **11**, 173 (2003).
[36] M. J. Cawkwell and T. D. Sewell (unpublished).
[37] R. Menikoff, Combust. Theory Modell. **12**, 73 (2008).
[38] H. H. Cady, J. Chem. Eng. Data **17**, 369 (1972).
[39] R. Menikoff, in *Shock Wave Science and Technology Reference Library*, edited by Y. Horie (Springer, New York, 2007), Vol. 2, p. 143.
[40] M. R. Baer, M. L. Hobbs, C. A. Hall, D. E. Hooks, R. L. Gustavsen, D. M. Dattelbaum, and S. A. Sheffield, in *Shock Compression of Condensed Matter—2007*, edited by M. D. Furnish, M. L. Elert, R. Chau, N. C. Holmes, and J. Nguyen (American Institute of Physics, Melville, NY, 2008), p. 1165.
[41] D. Cremer and J. A. Pople, J. Am. Chem. Soc. **97**, 1354 (1975).
[42] I. F. Shishkov, L. V. Vilkov, M. Kolonits, and B. Rozsondai, Struct. Chem. **2**, 57 (1991).
[43] N. J. Harris and K. Lammertsma, J. Am. Chem. Soc. **119**, 6583 (1997).
[44] J. B. Maillet, M. Mareschal, L. Soulard, R. Ravelo, P. S. Lomdahl, T. C. Germann, and B. L. Holian, Phys. Rev. E **63**, 016121 (2000).
[45] E. J. Reed, L. E. Fried, and J. D. Joannopoulos, Phys. Rev. Lett. **90**, 235503 (2003).
[46] R. Ravelo, B. L. Holian, T. C. Germann, and P. S. Lomdahl, Phys. Rev. B **70**, 014103 (2004).
[47] E. J. Reed, M. R. Manaa, L. E. Fried, K. R. Glaesemann, and J. D. Joannopoulos, Nat. Phys. **4**, 72 (2008).
[48] T. D. Sewell, D. L. Thompson, J. D. Gezelter, and W. H. Miller, Chem. Phys. Lett. **193**, 512 (1992).
[49] Y. Guo, D. L. Thompson, and T. D. Sewell, J. Chem. Phys. **104**, 576 (1996).
[50] A. Strachan and B. L. Holian, Phys. Rev. Lett. **94**, 014301 (2005).